ACS EARTH AND SPACE CHEMISTRY

Article

http://pubs.acs.org/journal/aesccq

Reaction Kinetics of CaOH with H and O_2 and O_2CaOH with O: Implications for the Atmospheric Chemistry of Meteoric Calcium

Juan Carlos Gomez Martin and John M. C. Plane*

School of Chemistry, University of Leeds, Leeds LS2 9JT, United Kingdom

Supporting Information

ABSTRACT: The ablation of cosmic dust particles entering the Earth's upper atmosphere produces a layer of Ca atoms around 90 km. Here, we present a set of kinetic experiments designed to understand the nature of the Ca molecular reservoirs on the underside of the layer. CaOH was produced by laser ablation of a Ca target in the fast flow tube and detected by non-resonant laser-induced fluorescence, probing the $D(^2\Sigma^+) \leftarrow X(^2\Sigma^1)$ transition at 346.9 nm. The following rate constants were measured (at 298 K): $k(CaOH + H \rightarrow Ca + H_2O) = (1.04 \pm 0.24) \times 10^{-10}$ cm^3 molecule^{-1} s^{-1}, $k(CaOH + O \rightarrow CaO + OH) < 1 \times 10^{-11}$ cm^3 molecule^{-1} s^{-1}, and $k(CaOH + O_2 \rightarrow O_2CaOH, 1\ Torr) = (5.9 \pm 1.8) \times 10^{-11}$ cm^3 molecule^{-1} s^{-1} (uncertainty at the 2σ level of confidence). The recycling of CaOH from reaction between O_2CaOH and O proceeds with an effective rate constant of $k_{eff}(O_2CaOH + O \rightarrow CaOH + products, 298\ K) = 2.8^{+2.0}_{-1.2} \times 10^{-10}$ cm^3 molecule^{-1} s^{-1}. Master equation modeling of the CaOH + O_2 kinetics is used to extrapolate to mesospheric temperatures and pressures. The results suggest that the formation of O_2CaOH slows the conversion of CaOH to atomic Ca via reaction with atomic H, and O_2CaOH is likely to be a long-lived reservoir species on the underside of the Ca layer and a building block of meteoric smoke particles.

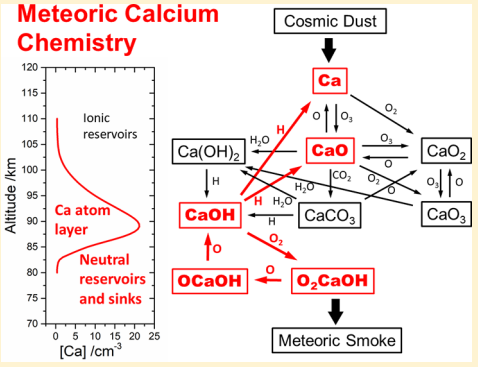

KEYWORDS: *gas-phase metal chemistry, laser spectroscopy, calcium hydroxide, mesosphere–lower thermosphere, meteoric calcium layer*

1. INTRODUCTION

Layers of metal atoms occur in the mesosphere–lower thermosphere (MLT) region of the Earth's atmosphere as a result of the ablation of cosmic dust particles. The total input of this dust has recently been estimated to be 43 ± 14 tonnes day^{-1}, of which around 92% comes from comets and the rest comes from the asteroid belt between Mars and Jupiter.[1] The ablated metal atoms occur in layers between 80 and 105 km, which are global in extent. Four neutral metal atoms, Na, Fe, K, and Ca, can be observed from the Earth's surface using the resonant lidar technique; uniquely for ground-based observations, the Ca^+ ion layer can also be observed and occurs ~5 km above the neutral Ca layer.[2] Although Ca has a similar elemental abundance to Na in meteorites, the Ca atom abundance in the MLT is roughly 2 orders of magnitude smaller than that of Na.[3−5] One reason for this Ca depletion is the highly refractory nature of CaO in molten meteoroids,[6] so that Ca ablates about 1 order of magnitude less efficiently than Na.[1] We have recently confirmed this differential ablation using a novel meteoric ablation simulator.[7]

A second reason for the Ca depletion may be that Ca is converted to very stable reservoir species, which are less easy to recycle back to atomic Ca than the corresponding Na reservoir, $NaHCO_3$.[8] A good understanding of the cycling between elemental Ca and its reservoirs, including Ca-bearing ions, is emerging.[9−11] However, there is still a great deal of uncertainty about the nature of the stable Ca reservoirs. This is important because the formation of these reservoirs governs the lower ledge of meteoric atomic layers and, in some cases, may even determine the seasonal behavior of the layer as a whole.[12] Also, these processes determine the way in which metals incorporate into meteoric smoke particles (MSPs), which are nanometer-sized particles that form from the condensation of metallic species in the MLT.[2]

Figure 1 is a schematic diagram of calcium chemistry in the MLT. Ca atoms react with O_3 to produce CaO[13]

$$Ca + O_3 \rightarrow CaO + O_2 \quad (\Delta H_r = -295 \pm 17\ kJ\ mol^{-1}) \qquad (R1)$$

which can then be recycled back to Ca by reaction with $O(^3P)$ or further react to yield reservoir molecules.[10,14]

$$CaO + H_2O + M \rightarrow Ca(OH)_2 + M \quad (\Delta H_r = -390 \pm 40\ kJ\ mol^{-1}) \qquad (R2a)$$

$$CaO + CO_2 + M \rightarrow CaCO_3 + M \quad (\Delta H_r = -247\ kJ\ mol^{-1}) \qquad (R3)$$

Received: June 21, 2017
Revised: July 11, 2017
Accepted: July 14, 2017
Published: July 14, 2017

DOI: 10.1021/acsearthspacechem.7b00072
ACS Earth Space Chem. 2017, 1, 431−441

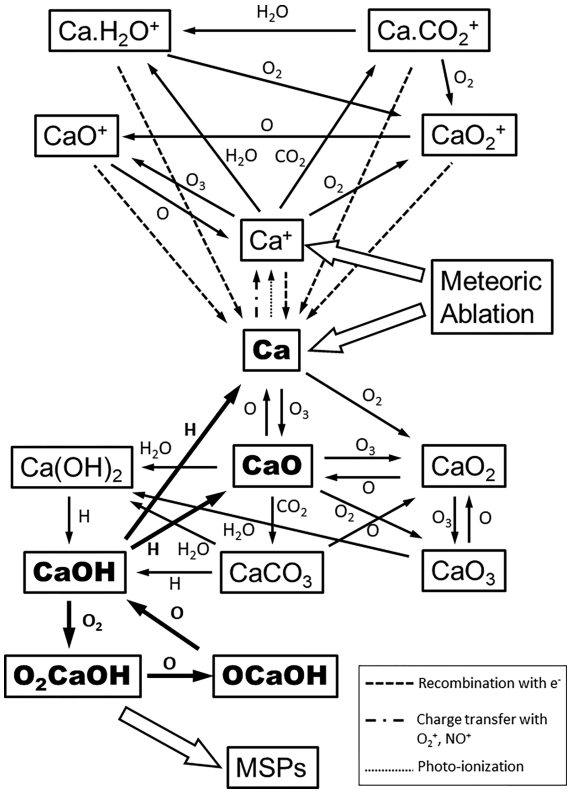

Figure 1. Meteoric calcium chemistry in the MLT. Bold typescript and thick arrows highlight the reactions investigated in this study.

$$CaCO_3 + H_2O \rightarrow Ca(OH)_2 + CO_2$$
$$(\Delta H_r = -148\ \text{kJ mol}^{-1}) \quad \text{(R4)}$$

Although $Ca(OH)_2$ is thermodynamically very stable, it reacts rapidly with H atoms to yield CaOH.[10]

$$Ca(OH)_2 + H \rightarrow CaOH + H_2O$$
$$(\Delta H_r = -20 \pm 40\ \text{kJ mol}^{-1}) \quad \text{(R5)}$$

The role of the CaOH radical as a reservoir species is the focus of the present study. CaOH can recycle back to Ca via a reaction that is well-known in the field of metal-catalyzed flame chemistry[15,16]

$$CaOH + H \rightarrow Ca + H_2O$$
$$(\Delta H_r = -108 \pm 15\ \text{kJ mol}^{-1}) \quad \text{(R6a)}$$

$$CaOH + H \rightarrow CaO + H_2$$
$$(\Delta H_r = -20 \pm 22\ \text{kJ mol}^{-1}) \quad \text{(R6b)}$$

where the combination of reactions R2a, R5, and R6b in essence catalyzes the recombination of 2H atoms to form H_2.

The reaction enthalpies at 0 K for reactions R1, R2a, R5, and R6 have been calculated using available heats of formation taken from data evaluations.[17−19] The preferred heats of formation of CaO and CaOH at 0 K (Figure S1 of the Supporting Information) are 26 ± 17 kJ mol^{-1} [19] and −170 ± 15 kJ mol^{-1},[17] respectively. Enthalpies of reaction for reactions R3 and R4 were obtained from electronic structure calculations at the B3LYP/6-311+(2d,p) level of theory (estimated uncertainty of ±20 kJ mol^{-1}).[10,14]

As shown in Figure 1, an unexplored and potentially important fate for CaOH could be its association with O_2 [enthalpies of reaction from B3LYP/6-311+(2d,p) calculations can be found in the Supporting Information].

$$CaOH + O_2 + M \rightarrow O_2CaOH + M$$
$$(\Delta H_r = -251\ \text{kJ mol}^{-1}) \quad \text{(R7)}$$

The O_2CaOH molecule can then recycle CaOH back by reaction with $O(^3P)$ in two steps

$$O_2CaOH + O \rightarrow OCaOH + O_2$$
$$(\Delta H_r = -133\ \text{kJ mol}^{-1}) \quad \text{(R8)}$$

$$OCaOH + O \rightarrow CaOH + O_2$$
$$(\Delta H_r = -161\ \text{kJ mol}^{-1}) \quad \text{(R9)}$$

or associate with other metal-containing molecules to generate MSPs.

The reaction of CaOH and O may also be slightly exothermic and could potentially recycle reactive calcium.

$$CaOH + O \rightarrow CaO + OH$$
$$(\Delta H_r = -13 \pm 22\ \text{kJ mol}^{-1}) \quad \text{(R10)}$$

In this paper, we investigate the atmospheric fate of CaOH by studying experimentally the reactions of CaOH with H and O_2 and the recycling of CaOH from O atom reactions.

2. EXPERIMENT

The laser ablation−fast flow tube−laser-induced fluorescence (LA−FFT−LIF) apparatus used in this study has been described in detail elsewhere.[20−22] Pulsed 532 nm Nd:YAG laser (Continuum Minilite) ablation of a rotating Ca cylindrical target was used to entrain Ca atoms and CaO molecules in a flow of a carrier gas, typically 3 standard liters per minute (slm) of N_2 at 2 Torr. Under these conditions, the linear flow speed was ∼30 m s^{-1}. A flow of H_2O or H_2 was added 2 cm downstream of the ablation source to generate CaOH (from electronically excited Ca species; see below). O_2 was added further downstream via a movable injector. The concentration of O_2 was changed by varying its flow while keeping the total flow constant by compensating with an extra flow of N_2. H atoms were generated by a microwave discharge (Opthos, 2450 MHz, Evenson cavity) of a flow of H_2 in He (1:5) and injected through a quartz tube at the midpoint between the ablation and the detection points, i.e., 10 cm downstream of the ablation point. The addition of He was essential to generate larger concentrations of H atoms. O atoms were generated by the microwave discharge of a flow of N_2 followed by scavenging of the resulting N atoms by an excess of NO downstream of the plasma and before injection into the flow tube.

H and O atom concentrations as a function of the microwave power were calibrated by adding a known excess concentration of NO_2 to the carrier flow upstream of the injector, to scavenge the corresponding atomic species via the well-known reactions:

$$NO_2 + H \rightarrow NO + OH \quad \text{(R11)}$$

$$NO_2 + O \rightarrow NO + O_2 \quad \text{(R12)}$$

NO_2 was monitored by electron impact−time-of-flight−mass spectrometry (EI−ToF−MS). The absolute difference in the NO concentration in the presence of atomic H or O, $\Delta[NO_2]$,

DOI: 10.1021/acsearthspacechem.7b00072
ACS Earth Space Chem. 2017, 1, 431−441

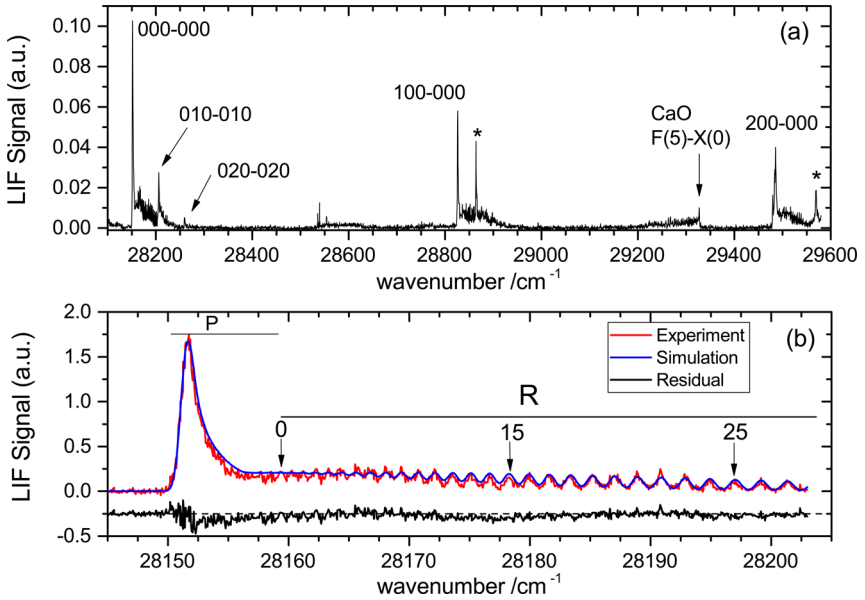

Figure 2. (a) Excitation spectrum showing ro-vibrational bands of the D−X transition of CaOH, with band assignments according to Pereira and Levy.[26] The red degraded band at 29 323 cm^{-1} fits well to the F(5)−X(0) transition of CaO, considering both the position of the band head and the spacing of the rotational lines. The prominent unassigned features (∗) also appear in the spectra by Pereira and Levy and show variable intensity with respect to the CaOH bands. (b) Detail of the D(000) ← X(000) band overlaid with a spectral simulation using molecular constants from Dick et al.[28] (*T*, 300 K; Doppler width, 1.1 cm^{-1}).

was calculated from the fractional change in the NO_2 signal and the known concentration of NO_2 added to the flow; $\Delta[NO_2] = [H]_0$ or $[O]_0$, their concentrations at the point of injection. The skimmer cone of the EI−ToF−MS was situated at the downstream end of the flow tube, 26 cm away from the microwave discharge. To measure the wall loss rate of H and O, NO_2 was injected at different distances downstream of the microwave discharge port by changing the position of a movable injector. The residence time of the atoms in the tube could thus be varied before titration with NO_2, so that the drop of the NO_2 concentration observed is equal to the remaining concentration of H or O in the tube after a given flight time in the absence of reagents. The maximum concentrations of H and O atoms that were generated using this methodology were about 3×10^{13} atoms cm^{-3}.

The relative CaOH concentration was measured 20 cm downstream of the ablation target by LIF between 336 and 356 nm, generated by directing a laser orthogonal to the flow tube axis. Pulsed laser radiation (pulse width, 6 ns; line width, 0.003 nm) was generated by a Nd:YAG-pumped dye laser (Continuum Surelite−Sirah Cobra Stretch) running on a solution of pyridine 1 in ethanol and frequency doubled with a KDP crystal. CaOH off-resonance fluorescence was collected perpendicular to the excitation beam through an orange high pass filter (Edmund Scientific, cuton at 550 nm) by a photomultiplier tube (Electron Tubes, 9816QB). Excitation of ro-vibrational bands of the $D(^2\Sigma^+) \leftarrow X(^2\Sigma^1)$ transition was followed by green−orange fluorescence from the $B(^2\Sigma^+) \rightarrow X(^2\Sigma^+)$ and $A(^2\Pi) \rightarrow X(^2\Sigma^1)$ transitions[23] (Figure 2a). In kinetic experiments, the CaOH concentration was monitored at the band head of the 100 ← 000 transition (346.88 nm vacuum or 28 848 cm^{-1}; Figure 2b). The incident laser energy was monitored using a beamsplitter and photodiode, so that the LIF signal could be corrected for the pulse-to-pulse laser variability. A wavemeter (Bristol Instruments 871B) was used to monitor the wavelength of the excitation beam during spectral scans. The signals from the different detectors were recorded using a digital oscilloscope (LeCroy LT342) and transferred to a computer for further analysis. The laser triggering, oscilloscope data acquisition, and cycle repetition were synchronized using a delay generator (Quantum Composers 9815).

2.1. Materials. OFN N_2 and UHP He (BOC) were used as carrier gases in the flow tube and the microwave discharge, respectively. Both N_2 and He passed through liquid N_2-cooled molecular sieve filters upstream of the experiment. UHP O_2 and H_2 (BOC) were used directly from the cylinder or from a glass bulb containing O_2 diluted in N_2 to a set partial pressure. NO_2 (Air Products, 99.5%) was frozen at 77 K, pumped, thawed, and stored in a glass bulb, where it was diluted in N_2 to make a 10% mixture. NO (99.95%, Air Products) was purified by freezing at 77 K, then warming the solid back to room temperature, and discarding the last 20% to vaporization. This process was repeated 3 times, and resulting NO was diluted in N_2 to make a 3% mixture. A Ca ablation target (diameter = 6 mm) was prepared by compressing Ca pellets (99%, Sigma-Aldrich) into a cylindrical shape using a stainless-steel piston.

3. RESULTS

3.1. Removal of Ca and CaO and Formation of CaOH. In the absence of reagents, laser ablation of the calcium target produced not only Ca atoms but also ground-state CaO and CaOH (both oxidation and hydration must occur during the preparation of samples under atmospheric conditions). Emission of blueish fluorescence around the ablation target indicated the formation of excited Ca. This emission was dispersed using a small monochromator, revealing many Ca lines between 300 and 600 nm, most of them connecting to the $^3P^\circ_J$ optically metastable state (181 kJ mol^{-1} above the ground ^1S state[24]). The resonance line at 422.673 nm was not the strongest of these lines. At the LIF detection point, 20 cm downstream of the ablation target, fluorescence from the $C(^1\Sigma^+) \leftarrow X(^1\Sigma^+)$ and $F(^1\Pi) \leftarrow X(^1\Sigma^+)$ band systems of

DOI: 10.1021/acsearthspacechem.7b00072
ACS Earth Space Chem. 2017, 1, 431−441

CaO[25] and the D($^2\Sigma^+$) ← X($^2\Sigma^+$) band system of CaOH[26] was observed by scanning the dye laser wavelength. The ground-state CaO signals were greatly diminished or disappeared upon addition of H_2 or H_2O, while the signal at the peak of the CaOH D(100)−X(000) band increased correspondingly by about a factor of 6 (signal slightly larger with H_2O than with H_2). Figure 2a shows a spectral scan obtained using H_2O as a reagent at 2 Torr. Figure 2b shows a comparison of the D(000) ← X(000) band of CaOH with a synthetic spectrum at 300 K calculated using the PGOPHER program,[27] with literature molecular constants.[28] The comparison demonstrates that the rotational state population is consistent with a rotational temperature of 300 K. The relative intensities of the (0, v_2', 0) ← (0, v_2'', 0) vibrational bands in Figure 2a also indicate a vibrational temperature of 300 K.

Some experiments were carried out to investigate the source of CaO and CaOH. Figure 3 shows the respective appearance and removal of ground-state CaOH (panel a) and CaO (panel b) with increasing H_2. The LIF signal at the peak of the CaOH bands shows evidence of overlap with the CaO[F(5)−X(0)] bands when no reagent is added. As the concentration of H_2 or H_2O is increased, the CaO signal decays exponentially. The signal at the peak of the CaOH D(100)−X(000) band can be fitted using a bi-exponential expression (solid line), where the initial decay constant ($k \sim 1 \times 10^{-10}$ cm^3 molecule^{-1} s^{-1}) is close to the decay constant of the single exponential fit of CaO in the bottom panel. This suggests that a fraction of CaOH originates initially from CaO. CaOH also shows a slower growth with increasing [H_2] ($k \sim 2 \times 10^{-10}$ cm^3 molecule^{-1} s^{-1}). This slower source is ultimately responsible for most of the CaOH signal observed under the usual experimental conditions, where [H_2] was 10 times higher than the maximum [H_2] in Figure 3 (~3×10^{13} molecules cm^{-3}), i.e., the aforementioned factor of 6 increase. The decay of CaO (Figure 3b) in this set of low [H_2] experiments was observed to depend upon the contact time, approaching the literature values of k(CaO + H_2) and k(CaO + H_2O)[10,14] when H_2 and H_2O are injected closer to the ablation target.

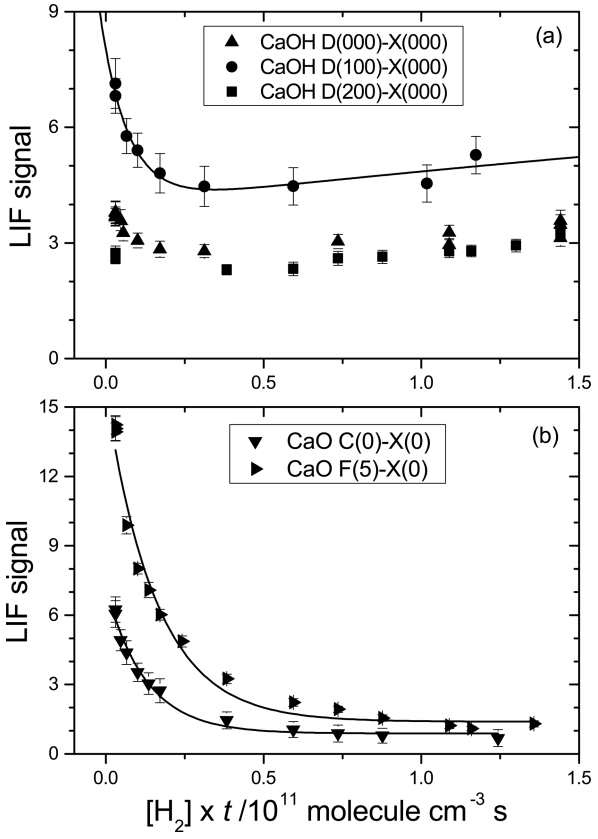

Figure 3. (a) Dependence of the CaOH LIF signals at the peak of three different bands of the D−X system on the concentration of [H_2] (multiplied by a constant contact time t). (b) Same for the C−X and F−X systems of CaO. The CaOH traces show, in fact, an overlap of the CaO and CaOH signal. This spectral overlap can be appreciated in Figure 4c; λ = 693.3−693.8 nm. For very low [H_2] (or [H_2O]), the signal at the peak of the CaOH bands shows a decay with the same constant as the decay of CaO in panel b. The degree of overlap varies for the other two bands shown in panel a. The slower growth of CaOH that can be appreciated in panel a is ultimately responsible for the formation of most CaOH that is observed in experiments of CaOH reactions, where the concentration of H_2 is 10 times higher.

Ca was observed by EI−ToF−MS at m/z 40, 42, and 44 and decayed exponentially to a very small baseline (less than 10% of the initial Ca) upon the addition of increasing water concentrations, with a rate constant of k = (1.0 ± 0.2) × 10^{-11} cm^3 molecule^{-1} s^{-1}. CaOH was also detected in the mass spectra at m/z 57, exhibiting the formation and subsequent decay with increasing [H_2O], although the signal was too noisy to allow for kinetic analysis. The addition of H_2 did not remove the Ca signal. In the absence of any reagent, at pressures below 1 Torr and with the same total flow rate (and, therefore, flow speeds faster by a factor of 2 and reduced collisional quenching), fluorescence was observed at the LIF detection point without excitation, showing the characteristic time variation of the ablation pulse (see, e.g., the study by Broadley et al.[11]). This emission was spectrally bracketed using high pass filters between 600 and 700 nm.

3.2. CaOH + H. Reaction R6 (with H in excess over CaOH) and the first-order loss of CaOH and H to the flow tube wall can be described by the following set of differential equations:

$$\frac{d[H]}{dt} = -k'_H[H] \quad \text{(E1)}$$

$$\frac{d[CaOH]}{dt} = -k_6[H][CaOH] - k'_{CaOH}[CaOH] \quad \text{(E2)}$$

where k'_H and k'_{CaOH} are the wall loss rates of H and CaOH, respectively. The main assumption here is that no additional sources of CaOH exist, i.e., that CaOH is not recycled from the products of reaction R6. The time dependence of CaOH is then described by an analytical solution of eqs E1 and E2

$$[CaOH] = [CaOH]_0 \exp(-(1 - \exp(-k'_H t))k'_H{}^{-1}k_6[H]_0 - k'_{CaOH}t) \quad \text{(E3)}$$

where $[H]_0$ is the initial concentration of H, i.e., the concentration at the injection point. Measurements were performed at a fixed contact time t defined by the mass flow rate of the carrier gas and the pressure in the flow tube. These experimental settings also determine the diffusional loss of H toward the wall, which was measured after the discharge calibration experiments and prior to the CaOH + H experiments. Therefore, eq E3 can be rewritten as

$$S_{CaOH} = A \exp(-k_6\tau[H]_0) \quad \text{(E4)}$$

DOI: 10.1021/acsearthspacechem.7b00072
ACS Earth Space Chem. 2017, 1, 431−441

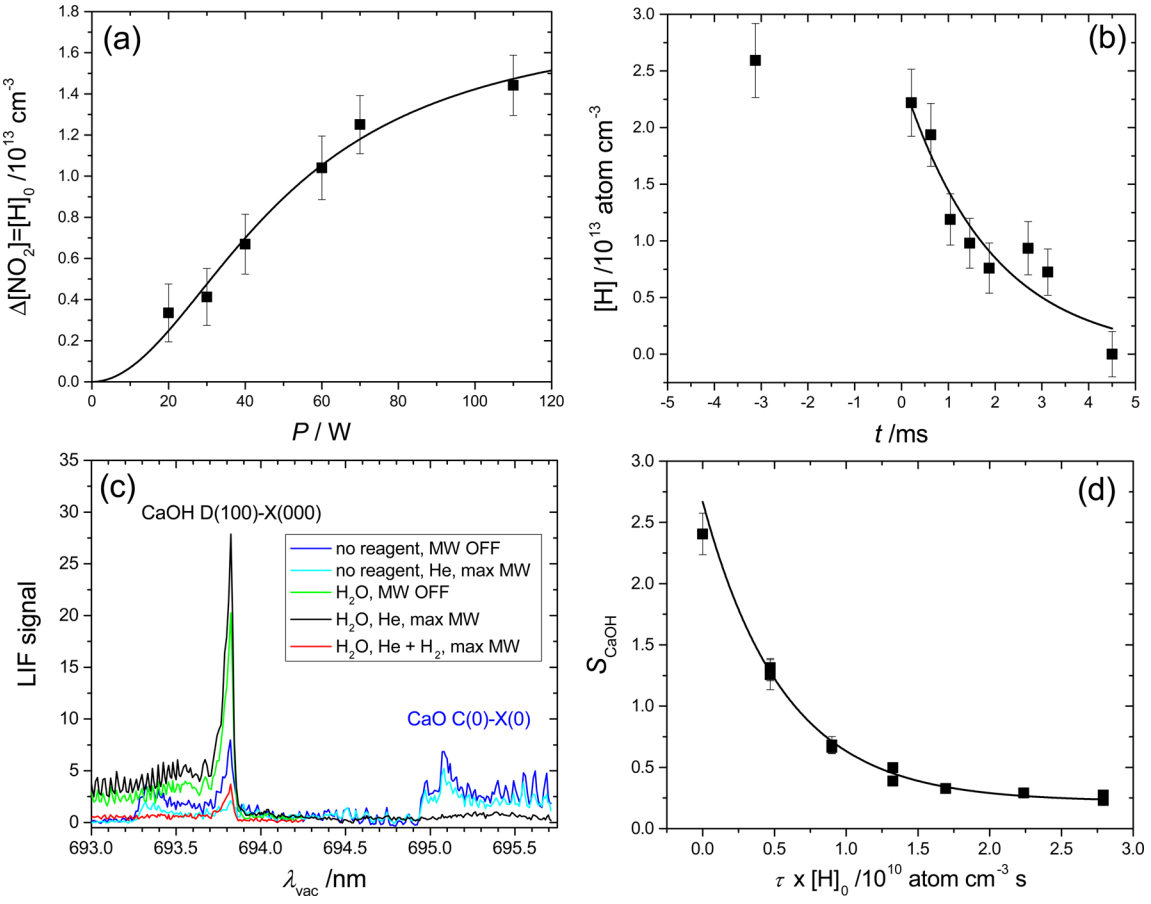

Figure 4. Example of the sequence of experiments carried out to determine the rate constant of the CaOH + H reaction. (a) H atom calibration of the MW discharge, showing $\Delta[NO_2]$ versus discharge power. (b) Loss of H atoms versus flight time, as determined by the distance between the MW port and the tip of the NO_2 movable injector. (c) Excitation spectra in the absence of added reagent with and without discharge on He (blue and cyan, respectively), in the presence of H_2O added downstream of the ablation point with and without discharge on He (black and green, respectively), and with H_2O added and the maximum H atom concentration for these particular conditions (red). (d) Plot of the CaOH LIF signal at the D(100)−X(000) bandhead versus the product of the effective contact time τ (see the text for definition) and the initial H atom concentration $[H]_0$.

Table 1. Measured Rate Constants for the CaOH + H Reaction at 298 K

reactant	flow (slm)	P (Torr)	t (ms)	k'_H (s^{-1})	k_6[a] ($\times 10^{-10}$, cm^3 $molecule^{-1}$ s^{-1})
H_2O	2.5	2.0	4.0 ± 0.3	430 ± 80	2.2 ± 0.9
H_2O	3.8	2.0	2.63 ± 0.17	430 ± 80	2.1 ± 0.9
H_2O	4.7	2.0	2.13 ± 0.13	620 ± 40	1.0 ± 0.5
none	4.7	2.0	2.13 ± 0.13	620 ± 40	1.6 ± 0.6
H_2O	4.7	2.0	2.13 ± 0.13	700 ± 100	1.2 ± 0.5
H_2O	2.6	1.7	3.3 ± 0.3	703 ± 120	0.9 ± 0.3
H_2O	2.3	2.0	4.2 ± 0.4	680 ± 50	0.8 ± 0.3
H_2O	2.3	2.0	4.2 ± 0.4	680 ± 50	1.0 ± 0.3
H_2O	2.3	1.0	2.13 ± 0.18	990 ± 120	0.9 ± 0.3
H_2O	2.6	0.6	1.23 ± 0.10	980 ± 150	2.1 ± 1.3
H_2	1.7	1.0	2.9 ± 0.3	950 ± 150	1.3 ± 0.4
weighted average					1.04 ± 0.12

[a]Random uncertainty at the 1σ level of confidence.

where S_{CaOH} is the observed CaOH LIF signal, A is a constant, and τ is an effective time calculated from the contact time t and the measured k'_H:

$$\tau = (1 - \exp(-k'_H t))k'_H{}^{-1} \quad \text{(E5)}$$

Figure 4 shows plots of S_{CaOH} versus $\tau[H]_0$ for different combinations of pressure and carrier flow. The exponential fits yield the total rate constant of reaction R6 ($k_6 = k_{6a} + k_{6b}$). Table 1 is a summary of the experiments carried out with different CaOH precursors and contact times. Additional back-to-back experiments using H_2O and H_2 as precursor reagents yielded the same dependence of S_{CaOH} upon $[H]_0$, suggesting that there are no interferences derived from recycling of CaOH from $Ca(OH)_2$ via reactions R2 and R5. The major sources of

DOI: 10.1021/acsearthspacechem.7b00072
ACS Earth Space Chem. 2017, 1, 431−441

uncertainty are the microwave (MW) discharge H atom calibration (~15%) and the H atom wall loss rate measurements (~30%). Another important source of uncertainty is the baseline that appears in most decays, about 10% of the initial CaOH LIF signal (see Figure 4d), both using H_2 and H_2O in the CaOH source. Because the H atom concentration does not depend linearly upon the discharge power but levels off at ~60 W (Figure 4a), it was not possible to increase [H] further to see whether CaOH would eventually disappear or the baseline would stay. In some cases, it was possible to fit the curves by fixing a zero baseline, and in these, the retrieved rate constant tends to hit the lower limit of the uncertainty range. It was found that discharging He without adding H_2 to the flow passing through the MW cavity created a small additional source of CaO when no H_2 or H_2O were added downstream of the ablation target (blue and cyan spectra in Figure 4c) and CaOH if a reagent was added downstream (black and green spectra in Figure 4c). Therefore, the additional source of CaO/CaOH appears to be associated with reactions involving oxides of calcium ablated directly from the source and excited He atoms generated by the MW discharge. The weighted average of the measurements in Table 1 yields a rate constant of $k_6(298\ \mathrm{K}) = (1.04 \pm 0.24) \times 10^{-10}$ cm^3 molecule^{-1} s^{-1} (uncertainty at the 2σ level of confidence).

3.3. CaOH + O_2. This reaction was studied by injecting O_2 into the flow tube at the MW discharge port (with the MW off). CaOH was generated as described above, using H_2O as the reagent. CaOH decayed upon the addition of increasing O_2 concentrations (Figure 5a). The decays were exponential up to 2 Torr and started to become bi-exponential at higher pressures. We speculate that the bi-exponential decays are related to excited carrier gas atoms (metastable triplet He atoms) generated in the MW discharge. The bimolecular rate constants (i.e., $k_{rec,7} = k_7[N_2]$) obtained from single-exponential fits at low pressures (0.5−2 Torr) or the fast component of the bi-exponential (2−5 Torr) fits increase with the pressure, as expected for reaction R7 (Figure 5b). The resulting values of $k_{rec,7}$ are listed in Table 2.

3.4. O_2CaOH + O. To study reactions R8 and R9, O_2CaOH was prepared by first injecting H_2O and then O_2 downstream of the ablation target (t = 0.3 and 1.6 ms after the ablation pulse, respectively) and upstream of the MW discharge port (t = 3.2 ms). The addition of O atom concentrations via the MW port resulted in the reappearance of a fraction of the CaOH LIF signal (detected at t = 6.4 ms) that had been lost by the addition of O_2 upstream of the O atom injection. The CaOH recovery was stronger for lower $[O_2]$ concentrations (Figure 6). This phenomenological growth of the CaOH signal with an increasing O concentration can be rationalized in terms of the chemical cycle formed by reactions R8−R9−R7. These reactions (with H in excess over O_2CaOH and OCaOH) together with the first-order losses of O_2CaOH, OCaOH, CaOH, and O to the walls of the flow tube are described by the following coupled differential equations:

$$\frac{d[O]}{dt} = -k'_O[O] \quad \text{(E6)}$$

$$\frac{d[O_2CaOH]}{dt} = -k_8[O][O_2CaOH] - k'_{O_2CaOH}[O_2CaOH] + k_{rec,7}[O_2][CaOH] \quad \text{(E7)}$$

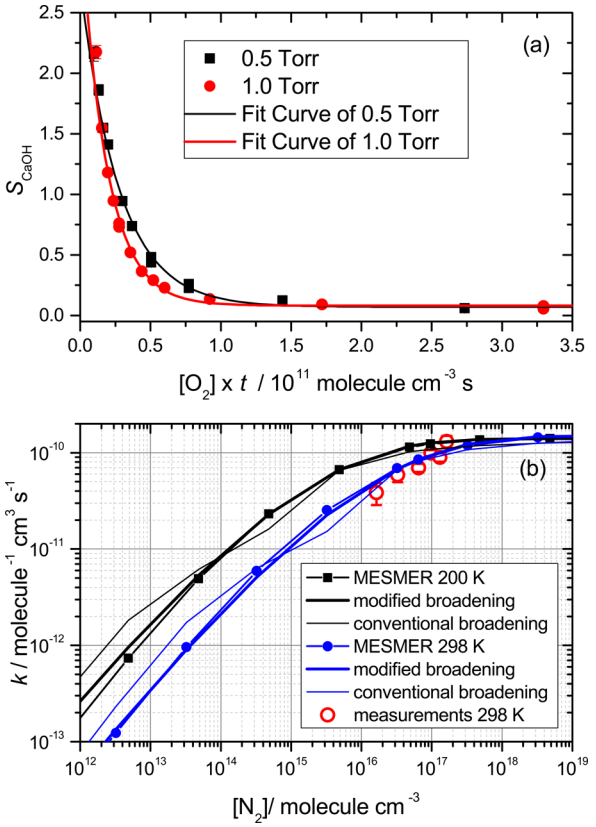

Figure 5. (a) Decay of the CaOH LIF signal with increasing $[O_2]$ for two buffer gas pressures. (b) Dependence of the bimolecular rate constant of CaOH removal by O_2 on the number density of the buffer gas (N_2). Red circles, experimental data at 298 K; blue dots and black squares, master equation calculations at 298 and 200 K, respectively; and thin and thick lines, fits to the master equation results to the Troe expression for termolecular reactions, using the conventional broadening factor[39] and the new broadening factors proposed in ref 41, respectively.

Table 2. Measured Rate Constants for the CaOH + O_2 + M Reaction at 298 K

flow (slm)	P (Torr)	t (ms)	$k_{rec,7}$[a] (×10^{-11}, cm^3 molecule^{-1} s^{-1})
0.7	0.5	4.0 ± 1.0	3.9 ± 1.0
1.1	1.0	4.5 ± 0.7	5.9 ± 0.9
2.5	2.0	4.0 ± 0.3	7.0 ± 0.9
3.8	3.0	4.0 ± 0.3	9.9 ± 0.8
5.6	4.0	3.58 ± 0.22	9.0 ± 0.9
7.0	5.0	3.86 ± 0.22	13.1 ± 1.9

[a]Random uncertainty at the 1σ level of confidence.

$$\frac{d[OCaOH]}{dt} = -k_9[O][OCaOH] - k'_{OCaOH}[OCaOH] + k_8[O][O_2CaOH] \quad \text{(E8)}$$

$$\frac{d[CaOH]}{dt} = -k_{rec,7}[O_2][CaOH] - k'_{CaOH}[CaOH] - k_{10}[O][CaOH] + k_9[O][OCaOH] \quad \text{(E9)}$$

where k'_O, k'_{O_2CaOH}, and k'_{OCaOH} are the wall loss rates of O, O_2CaOH, and OCaOH, respectively. The wall loss rate of atomic O was found to be $k'_O = 250 \pm 50$ s^{-1}. Theoretical estimates of the diffusion coefficients of Ca-containing

DOI: 10.1021/acsearthspacechem.7b00072
ACS Earth Space Chem. 2017, 1, 431−441

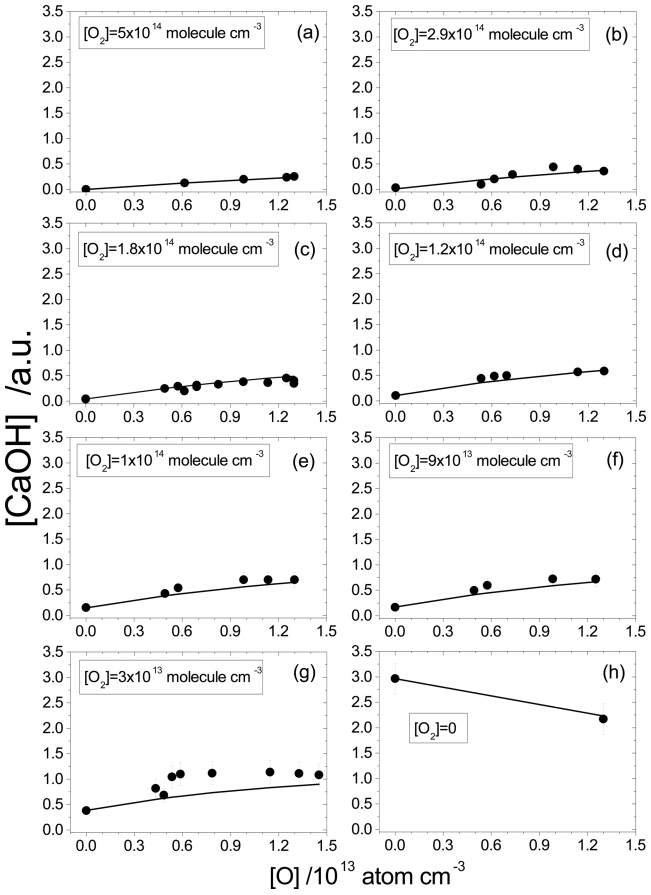

Figure 6. Reappearance of CaOH upon the addition of O atoms into a flow, where CaOH has been previously converted to O_2CaOH by an excess of O_2. Each panel (a–g) corresponds to a different O_2 concentration, in decreasing order. The CaOH level in the absence of O_2 and O (panel h) is placed at 3 units in the relative concentration scale shown. The solid lines are the optimal solution in the least squares sense of the system of differential eqs E6–E9, with $k_{eff} = 5.5 \times 10^{-11}$ cm^3 molecule^{-1} s^{-1}. Almost identical simulated curves are obtained by modeling explicitly reactions R8 and R9, with $k_8 = 5.4 \times 10^{-11}$ cm^3 molecule^{-1} s^{-1} and $k_9 = 1.1 \times 10^{-10}$ cm^3 molecule^{-1} s^{-1}.

molecules, such as CaOH, $Ca(OH)_2$, or CaO_3, in N_2[10] justify using a common first-order loss rate k'_{CaX} for CaOH, OCaOH, and O_2CaOH, which greatly simplifies the modeling of eqs E6–E9; i.e., $k'_{CaX} = k'_{CaOH} = k'_{OCaOH} = k'_{O_2CaOH}$.

In eq E9, a term has been included for reaction R10. It is likely that reaction R10 cannot compete with reaction R7 because $[O_2] \gg [O]$, and reaction R7 at 2 Torr is not far from the gas kinetic rate constant (see below); however, reaction R10 might become competitive when $[O_2] \sim [O]$. To test this possibility, experiments were carried out where O atoms were added to the flow carrying CaOH in the absence of O_2. Removal of CaOH was only observed beyond experimental uncertainty (Figure 6h) for the maximum O atom concentration that could be reached ($[O] \sim 1.3 \times 10^{13}$ atom cm^{-3}), implying an upper limit to the rate constant for reaction R10 of $k_{10} \leq 1 \times 10^{-11}$ cm^3 molecule^{-1} s^{-1}.

The system of differential eqs E6–E9 was integrated numerically, and the resulting calculated curves of [CaOH] versus [O] for different $[O_2]$ were fitted to the observed S_{CaOH} LIF versus [O] and $[O_2]$ by floating the rate constants k_8 and k_9 using a nonlinear least squares method.[10] However, Figure 7

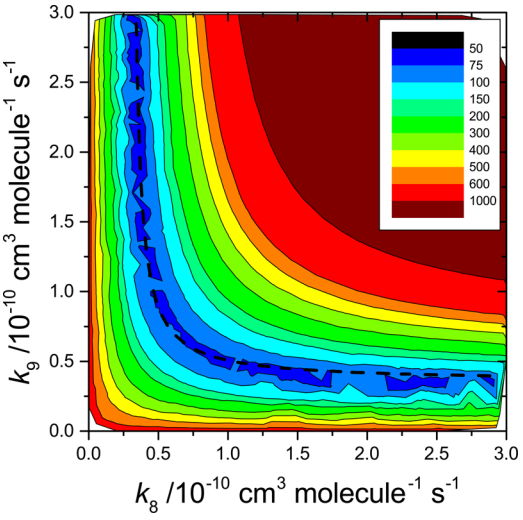

Figure 7. Contour plot of the sum of error-weighted squared residuals (χ^2) (residuals calculated as the difference between the data in Figure 6 and numerical solutions to the system of differential eqs E6–E9 with different values of k_8 and k_9) versus the free parameters k_8 and k_9. The dashed line indicates the empirical dependence of k_9 versus k_8 in the region with $\chi^2 < 80$, given by $k_9 = 3.5 \times 10^{-11} k_8/(k_8 - 3.0 \times 10^{-11})$.

shows that the sum of squared residuals χ^2 does not present a well-defined minimum for k_8 and k_9. These parameters are highly correlated, showing an empirical dependence (dashed line in Figure 7) that can be approximated by the following equation:

$$k_9 = 3.5 \times 10^{-11} k_8/(k_8 - 3.0 \times 10^{-11}) \quad \text{(E10)}$$

The asymptotes of this empirical dependence between the optimal values of k_8 and k_9 indicate a lower limit for both rate constants of 3×10^{-11} cm^3 molecule^{-1} s^{-1}. Alternatively, an effective reaction between O_2CaOH and O, leading directly to the CaOH product, can be considered. The effective rate constant obtained from a global fit to the data shown in Figure 6 using the latter approach is $k_{eff} = 2.8^{+2.0}_{-1.2} \times 10^{-11}$ cm^3 molecule^{-1} s^{-1}, where the uncertainty at 95% confidence encompasses uncertainty propagated from k'_O, k_{10}, the contact time t, and the concentrations of reagents. The uncertainty limits of k_{eff} also apply to the rate-limiting step.

4. DISCUSSION

4.1. Formation Mechanism of CaOH. The formation of CaOH from the evaporation[29] or ablation[26] of Ca within a carrier gas flow containing water vapor is well-known, but the actual mechanisms leading to CaOH have not been investigated in detail. In our LA–FFT–LIF experiments, the formation of CaOH in the gas phase requires the intervention of electronic excited states of Ca or CaO, because the reactions of Ca and CaO with H_2O to make CaOH are endothermic.[17,30]

$$Ca + H_2O \rightarrow CaOH + H \quad (\Delta H_r = 108 \pm 15 \text{ kJ mol}^{-1}) \quad \text{(R–6a)}$$

$$CaO + H_2O \rightarrow CaOH + OH \quad (\Delta H_r = 80 \pm 22 \text{ kJ mol}^{-1}) \quad \text{(R2b)}$$

The reaction of CaO and H_2 (reaction R–6b) to make CaOH is probably endothermic ($\Delta H_r = 20 \pm 22$ kJ mol^{-1}), although

DOI: 10.1021/acsearthspacechem.7b00072
ACS Earth Space Chem. 2017, 1, 431–441

the uncertainty is large because the uncertainties in the enthalpies of formation of CaO and CaOH are considerable (17 and 15 kJ mol^{-1}, respectively). The blue emission around the ablation target shows that Ca-bearing species are vaporized in highly excited states. The low-lying excited states Ca($^3P^\circ_J$, ^3D_J, $^1D_2$)[24] and CaO($A^1\Sigma^+$, $b^3\Sigma^+$, $a^3\Pi$, $A'^1\Pi$)[31] have sufficient energy to form CaOH from these reactions. Some of these states are also optically metastable, which increases the probability of reaction. The radiative lifetime of Ca(^3P_J) is 0.33 ms,[32] and the mean radiative lifetime of Ca($^1D_2$) for emission to all lower states, including Ca(^3P_J), is 1.7 ms.[32,33] The radiative lifetime of CaO($A'^1\Pi$) has not been measured but has been estimated to be on the order of 0.1 ms.[34]

The fact that similar amounts of CaOH are produced by the addition of H_2O and H_2 indicates that, in our experiments, the major precursor of CaOH must be an oxygen-bearing species: CaO* + H_2O/H_2. Minor contributions of Ca* + H_2O and possibly of CaO + H_2 depending upon the added reagent cannot be ruled out. Ground-state CaO is removed by H_2O via reaction R2a,[14] and by H_2[10] via

$$\mathrm{CaO} + \mathrm{H_2} \rightarrow \mathrm{Ca} + \mathrm{H_2O} \quad (\Delta H_r = -102 \pm 10\ \mathrm{kJ\ mol^{-1}}) \qquad \text{(R13)}$$

Because the initial rate of formation of CaOH is compatible with the CaO loss rate (Figure 3), it is possible that reaction R−6b does indeed occur (which supports the thermoneutrality of reaction R6b). However, this is a minor source of CaOH in our experiments, because when [H_2] is increased by up to a factor of 10, the CaOH LIF signal still grows by up to a factor of 6, long after any CaO has been removed.

The removal of CaO by H_2 has been seen to proceed with a slower rate constant (1×10^{-10} cm^3 molecule^{-1} s^{-1}) than the previously published result $k_{13} = (3.4 \pm 1.3) \times 10^{-10}$ cm^3 molecule^{-1} s^{-1}[10] and to slow when H_2 or H_2O are injected further away from the ablation target. CaO* collisional and radiative relaxation is most likely the cause of this observation. In competition with collisional quenching and radiative decay, CaO* reacts with H_2 or H_2O to form CaOH with a relatively slow rate constant of the order of 2×10^{-12} cm^3 molecule^{-1} s^{-1} (Figure 3). When sufficient amounts of reagent are added, most CaO* is converted to CaOH.

The spontaneous emission between 600 and 700 nm observed at a low pressure in the absence of reagents must correspond to a species with a radiative lifetime commensurate with ∼2.4 ms required to travel from the ablation target to the detection region (at the minimum pressure of 0.7 Torr in our experiments). The $^3P_J \rightarrow {}^1S$ transition of Ca occurs at 657.278 nm, and the radiative lifetimes of Ca(^3P_J) and Ca($^1D_2$) are of the order of 1 ms. CaO($A'^1\Pi$) is also expected to be long-lived and to give rise to chemiluminescence in the observed range.[35]

Our observations indicate that, shortly after ablation, highly excited Ca atoms decay predominantly to the metastable ^3P_J state, which is long-lived enough not to undergo complete radiative relaxation (or collisional quenching) within 0.3 ms of flight time between ablation and the point where water was injected. Thus, the removal process observed by EI−ToF−MS is likely to be the following reaction:

$$\mathrm{Ca(^3P_J)} + \mathrm{H_2O} \rightarrow \mathrm{CaOH} + \mathrm{H} \qquad \text{(R14)}$$

with $k_{14} = (1.0 \pm 0.2) \times 10^{-11}$ cm^3 molecule^{-1} s^{-1}.

4.2. CaOH + H. We have determined a rate constant of reaction R6 at room temperature of $k_6(298\ \mathrm{K}) = (1.04 \pm 0.24) \times 10^{-10}$ cm^3 molecule^{-1} s^{-1}. A summary of previous determinations of k_6 is presented in Figure 8. Our value is

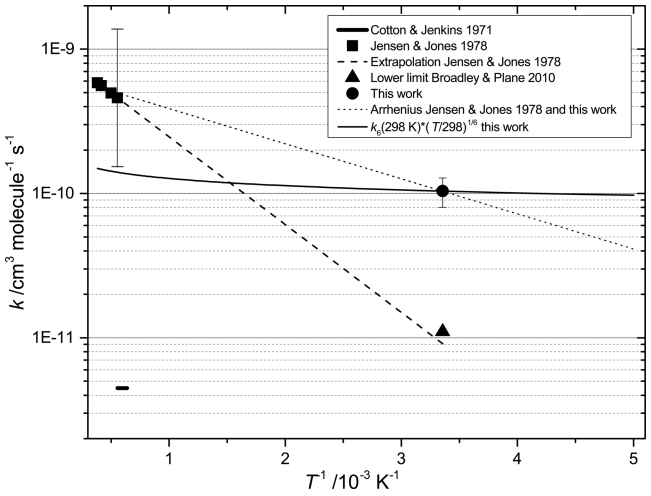

Figure 8. Literature values for the CaOH + H reaction and possible extrapolations toward low temperature. The dashed line is an extrapolation of the temperature-dependent expression reported by Jensen and Jones[16] between 1800 and 2615 K. The dotted line results from an Arrhenius fit to the 1978 flame data combined with the room-temperature determination reported in the present work. The thin solid line illustrates a long-range-type temperature dependence of $T^{1/6}$ to the room-temperature result of the present work.

consistent with the lower limit reported by Broadley and Plane:[10] $k_6(298\ \mathrm{K}) \geq 1.1 \times 10^{-11}$ cm^3 molecule^{-1} s^{-1}. Cotton and Jenkins[15] carried out a study of alkaline-earth-catalyzed radical recombination reactions in flames and found k_6(1570−1800 K) = 4.48×10^{-12} cm^3 molecule^{-1} s^{-1} (no uncertainty reported). In a subsequent flame study, Jensen and Jones[16] reported an Arrhenius expression k_6(1800−2615 K) = 1×10^{-9} exp(−1400/T) cm^3 molecule^{-1} s^{-1}, with an estimated uncertainty of a factor of 3. This expression is clearly at odds with the results of the earlier flame study. Extrapolation to room temperature yields $k_6(298\ \mathrm{K}) \sim 9 \times 10^{-12}$ cm^3 molecule^{-1} s^{-1}, which is consistent with the lower limit reported by Broadley and Plane, within the uncertainty of the extrapolated flame data. Also, an Arrhenius type of expression may be fitted to the average of the temperature range of Jensen and Jones and the room-temperature value reported in this work: k_6(300−2615 K) = 6.78×10^{-10} exp(−560/T) cm^3 molecule^{-1} s^{-1}.

The calculated potential energy surface (PES) for this reaction (Figure S1 of the Supporting Information) shows that the barrier leading to channel reaction R6a is submerged well below the entrance channel. Therefore, the reaction can always proceed via reaction R6a, which would rule out a significant activation energy. The overall rate constant $k_6 = k_{6a} + k_{6b}$ is more likely to show a very weak temperature dependence, for example, a $T^{1/6}$ type of dependence characteristic of long-range interaction. Only a temperature-dependent branching ratio would result from the endothermicity of reaction R6b, with k_{6b} increasing at the expense of k_{6a} as the temperature increases.

It is possible that the higher rate constant at 1800−2615 K determined by Jensen and Jones[16] results from systematic errors in the data analysis. The quoted uncertainty of the flame

DOI: 10.1021/acsearthspacechem.7b00072
ACS Earth Space Chem. 2017, 1, 431−441

results is large, not least because several reactions with unknown rate coefficients and equilibrium constants needed to be included in the mechanism to fit the emission spectroscopy observations; also, important reactions may have been ignored, and several catalytic cycles can potentially fit the observations. Furthermore, the uncertainty in the rate constants may be too large to fit a temperature dependence in a relatively reduced temperature range (1800−2615 K), which then needs to be extrapolated toward much lower temperatures. We note that Jensen and Jones also reported the rate constants of reaction R2a [k_{2a}(1800−2615 K) = 8×10^{-10} cm^3 molecule^{-1} s^{-1}, factor of 2.3 uncertainty] and reaction R5 [k_5(1800−2615 K) = 1.4×10^{-11} exp(−600/T) cm^3 molecule^{-1} s^{-1}, factor of 2.3 uncertainty]. Both rate constants have been determined for 278 < T < 513 K in previous PLP−LIF and LA−FFT−LIF studies in our laboratory,[10,14] producing the following results: k_{2a}(298 K, 760 Torr) = 5.8×10^{-10} cm^3 molecule^{-1} s^{-1} (20% uncertainty) and k_5(298 K) ≥ 1.1×10^{-11} cm^3 molecule^{-1} s^{-1}. Therefore, the flame and flow tube determinations of k_{2a} are consistent, but extrapolating k_5 of Jensen and Jones to room temperature results in k_5(298 K) = 1.9×10^{-12} cm^3 molecule^{-1} s^{-1}, which is inconsistent with the flow tube data. This seems to indicate that the flame study by Jensen and Jones produced high-temperature rate constants, which are, within uncertainty, consistent with the lower temperature results, but the Arrhenius temperature dependences are most likely wrong or not applicable below 1800 K.

Finally, in view of the discussion above, we recommend an overall rate constant for reaction R6 under mesospheric conditions of k_6(200 K) = $(1.0 \pm 0.3) \times 10^{-10}$ cm^3 molecule^{-1} s^{-1}. The question whether reaction R6b is endothermic or not remains open. However, this would not be very relevant in the MLT, because any CaO produced via reaction R6b would mostly be converted into Ca by reaction with atomic O (reaction R16 below), because this species occurs at significant concentrations throughout a full diurnal cycle at altitudes above 82 km.[2]

4.3. CaOH + O_2. The Master Equation Solver for Multi-Energy Well Reactions (MESMER)[36,37] was used to extrapolate k_7 toward the lower end of the range of mesospheric temperatures and pressures (T ∼ 120 K, and P ∼ 10^{-4} Torr). The required molecular parameters of the species of interest and the zero-point-corrected energies at 0 K of the stationary points on the PES were calculated at the B3LYP/6-311+g(2d,p) level using the Gaussian 09 package[38] (Table S1 of the Supporting Information). This level of theory compares well to results obtained with more accurate methods (Tables S1 and S2 of the Supporting Information). In MESMER, the internal energies of the stationary points on the PES are divided into a contiguous set of grains (width of 100 cm^{-1}), each containing a bundle of rovibrational states. The density of these states is calculated using the *ab initio* vibrational frequencies and rotational constants. Each grain was then assigned a set of microcanonical rate coefficients for dissociation, which were determined using inverse Laplace transformation to link them directly to the high-pressure limiting recombination coefficient, which, here, we set to the gas kinetic rate constant with an assumed temperature dependence: $k_{7rec,\infty}$ = $1.5 \times 10^{-10} \times (T/298\ \mathrm{K})^{1/6}$ cm^3 molecule^{-1} s^{-1}. The microcanonical dissociation rate coefficients are then determined by a detailed balance. The exponential down model is used for describing collisional energy transfer probabilities. The energy transfer parameter ΔE_{down} is set to a typical value for N_2 of 300 cm^{-1}.

The results of these calculations are shown in Figure 5b. Although we have not attempted floating the parameters to fit the experimental data, it can be seen that the agreement is quite satisfactory. The calculated rate constants were then fitted to the Lindemann expression modified by a broadening factor F_c[39] to derive an analytical expression for k_7 ready to use in atmospheric modeling, as we have done in a previous work.[14] The low-pressure limiting rate coefficient, $\log_{10}(k_{7rec,0}$, cm^6 molecule^{-2} s^{-1}) = −(12.70 ± 0.04) − (4.986 ± 0.016)log T is obtained from the MESMER calculation. The best fit yields F_c = 0.136 ± 0.005, which is smaller than the value of 0.6 often assumed.[40] The O_2CaOH adduct has a relatively large number of low-frequency vibrational modes (see Table S1 of the Supporting Information), which tends to cause F_c in the conventional falloff expression to be less than 0.2, resulting in unphysical inflection points in the falloff curves[41] (thin lines in Figure 5b). We have therefore used the modified broadening factor expression of Troe (eqs 7 and 8 in ref 41, with parameters x_0 = 0.9, b = 0.25, and F_c = 0.2), which produces a better fit to the master equation data, as shown by the thick lines in Figure 5b.

4.4. O_2CaOH + O. The rate-determining reaction of the sequence reaction R8−R9 proceeds with a rate constant of 3×10^{-11} cm^3 molecule^{-1} s^{-1}, but from the modeling of the available data, it is not possible to tell whether the rate-limiting step is reaction R8 or R9. A possible solution to the ambiguity in the assignment of values to the rate constants k_8 and k_9 is suggested by comparing reactions R8 and R9 to the analogous reactions.[10]

$$\mathrm{CaO + O \rightarrow Ca + O_2} \quad (\Delta H_r = -96 \pm 17\ \mathrm{kJ\ mol^{-1}\ exp};\ -94\ \mathrm{kJ\ mol^{-1}\ B3LYP}) \tag{R15}$$

$$\mathrm{CaO_2 + O \rightarrow CaO + O_2} \quad (\Delta H_r = -170\ \mathrm{kJ\ mol^{-1}\ B3LYP}) \tag{R16}$$

CaO_2 has C_{2v} symmetry, and therefore, the terminal O_2 is arranged in a similar manner to O_2CaOH.[10] The rate constants of these reactions have been reported by Broadley and Plane:[10] k_{15}(298 K) = $3.1^{+2.0}_{-1.5} \times 10^{-10}$ cm^3 molecule^{-1} s^{-1}, and k_{16}(298 K) = $2.2^{+7.0}_{-1.4} \times 10^{-11}$ cm^3 molecule^{-1} s^{-1}. Thus, it is possible that, by analogy and following eq E10, k_9(298 K) = 2.4×10^{-10} cm^3 molecule^{-1} s^{-1} and k_8(298 K) = 3.5×10^{-11} cm^3 molecule^{-1} s^{-1}. In any case, for atmospheric modeling purposes, it is always possible to choose one of the rate constants and use eq E10 to derive the other. Reactions R15 and R16 show weak temperature dependences,[10] owing to the absence of barriers and the potential wells of the adducts not being deep enough with respect to the exit channels to allow for stabilization. For reactions R8 and R9, we have a similar situation and therefore would expect the rate constants k_8 and k_9 to show a weak temperature dependence.

5. CONCLUSION

In this work, we report rate constants of important Ca-bearing molecules with species relevant in the MLT region, which have not been measured before or have only been measured in flame chemistry studies, i.e., within a range of temperatures far from the atmospheric range. We provide recommended values of these rate constants under MLT conditions. We have identified an important Ca reservoir, O_2CaOH, which forms quickly as a

DOI: 10.1021/acsearthspacechem.7b00072
ACS Earth Space Chem. 2017, 1, 431−441

result of the fast recombination of CaOH with O_2 and the high atmospheric abundance of O_2. Above 82 km, where there are significant concentrations of atomic O, even during the night,[2] the formation of O_2CaOH will provide a holding cycle, which slows the conversion of CaOH back to active Ca via a reaction with H. Below 82 km, where the atomic O concentration falls off by orders of magnitude, O_2CaOH will become the major sink for Ca and the likely form in which it is incorporated into MSPs.

■ ASSOCIATED CONTENT

Supporting Information

The Supporting Information is available free of charge on the ACS Publications website at DOI: 10.1021/acsearthspacechem.7b00072.

CaO and CaOH thermochemical data evaluation (Figure S1), *ab initio* geometries, molecular parameters, and energies of relevant molecules (Tables S1 and S2), and comparison of experimental and theoretical enthalpies of reaction (Table S3) (PDF)

■ AUTHOR INFORMATION

Corresponding Author

*E-mail: j.m.c.plane@leeds.ac.uk.

ORCID

Juan Carlos Gomez Martin: 0000-0001-7972-085X

Notes

The authors declare no competing financial interest.

■ ACKNOWLEDGMENTS

This work was supported by the European Research Council (Project 291332, CODITA).

■ REFERENCES

(1) Carrillo-Sánchez, J. D.; Nesvorný, D.; Pokorný, P.; Janches, D.; Plane, J. M. C. Sources of cosmic dust in the Earth's atmosphere. *Geophys. Res. Lett.* **2016**, *43* (23), 11,979−11,986.

(2) Plane, J. M. C.; Feng, W.; Dawkins, E. C. M. The Mesosphere and Metals: Chemistry and Changes. *Chem. Rev.* **2015**, *115* (10), 4497−4541.

(3) Gerding, M.; Alpers, M.; von Zahn, U.; Rollason, R. J.; Plane, J. M. C. Atmospheric Ca and Ca^+ layers: Midlatitude observations and modeling. *J. Geophys. Res.* **2000**, *105* (A12), 27131−27146.

(4) Granier, G.; Jégou, J. P.; Mégie, G. Resonant lidar detection of Ca and Ca^+ in the upper atmosphere. *Geophys. Res. Lett.* **1985**, *12* (10), 655−658.

(5) Raizada, S.; Tepley, C. A.; Aponte, N.; Cabassa, E. Characteristics of neutral calcium and Ca^+ near the mesopause, and their relationship with sporadic ion/electron layers at Arecibo. *Geophys. Res. Lett.* **2011**, *38* (9), L09103.

(6) Vondrak, T.; Plane, J. M. C.; Broadley, S.; Janches, D. A chemical model of meteoric ablation. *Atmos. Chem. Phys.* **2008**, *8* (23), 7015−7031.

(7) Gómez-Martín, J. C.; Bones, D. L.; Carrillo-Sánchez, J. D.; James, A. D.; Trigo-Rodríguez, J. M.; Fegley, B., Jr.; Plane, J. M. C. Novel experimental simulations of the atmospheric injection of meteoric metals. *Astrophys. J.* **2017**, *836* (2), 212.

(8) Marsh, D. R.; Janches, D.; Feng, W.; Plane, J. M. C. A global model of meteoric sodium. *J. Geophys. Res.: Atmos.* **2013**, *118* (19), 11,442−11,452.

(9) Bones, D. L.; Gerding, M.; Höffner, J.; Martín, J. C. G.; Plane, J. M. C. A study of the dissociative recombination of CaO^+ with electrons: Implications for Ca chemistry in the upper atmosphere. *Geophys. Res. Lett.* **2016**, *43* (24), 12,333−12,339.

(10) Broadley, S. L.; Plane, J. M. C. A kinetic study of reactions of calcium-containing molecules with O and H atoms: Implications for calcium chemistry in the upper atmosphere. *Phys. Chem. Chem. Phys.* **2010**, *12* (31), 9094−9106.

(11) Broadley, S. L.; Vondrak, T.; Plane, J. M. C. A kinetic study of the reactions of Ca^+ ions with O_3, O_2, N_2, CO_2 and H_2O. *Phys. Chem. Chem. Phys.* **2007**, *9* (31), 4357−4369.

(12) Plane, J. M. C.; Feng, W.; Dawkins, E.; Chipperfield, M. P.; Höffner, J.; Janches, D.; Marsh, D. R. Resolving the strange behavior of extraterrestrial potassium in the upper atmosphere. *Geophys. Res. Lett.* **2014**, *41* (13), 4753−4760.

(13) Helmer, M.; Plane, J. M. C.; Allen, M. R. A kinetic investigation of the reaction Ca + O_3 over the temperature range 213−383 K. *J. Chem. Soc., Faraday Trans.* **1993**, *89* (5), 763−769.

(14) Plane, J. M. C.; Rollason, R. J. Kinetic Study of the Reactions of CaO with H_2O, CO_2, O_2, and O_3: Implications for Calcium Chemistry in the Mesosphere. *J. Phys. Chem. A* **2001**, *105* (29), 7047−7056.

(15) Cotton, D. H.; Jenkins, D. R. Catalysis of radical-recombination reactions in flames by alkaline earth metals. *Trans. Faraday Soc.* **1971**, *67* (0), 730−739.

(16) Jensen, D. E.; Jones, G. A. Alkaline Earth Flame Chemistry. *Proc. R. Soc. London, Ser. A* **1978**, *364* (1719), 509−535.

(17) Gurvich, L. V.; Veyts, I. V.; Alcock, C. B. *Thermodynamic Properties of Individual Substances*, 4th ed.; Hemisphere Publishing Corporation: New York, 1989.

(18) Chase, M. W., Jr. *NIST-JANAF Thermochemical Tables*, 4th ed.; American Institute of Physics: Woodbury, NY, 1998; Monograph 9.

(19) Pedley, J. B.; Marshall, E. M. Thermochemical Data for Gaseous Monoxides. *J. Phys. Chem. Ref. Data* **1983**, *12* (4), 967−1031.

(20) Self, D. E.; Plane, J. M. C. A kinetic study of the reactions of iron oxides and hydroxides relevant to the chemistry of iron in the upper mesosphere. *Phys. Chem. Chem. Phys.* **2003**, *5* (7), 1407−1418.

(21) Gómez Martín, J. C.; Garraway, S. A.; Plane, J. M. C. Reaction Kinetics of Meteoric Sodium Reservoirs in the Upper Atmosphere. *J. Phys. Chem. A* **2016**, *120* (9), 1330−1346.

(22) Gómez Martín, J. C.; Daly, S. M.; Brooke, J. S. A.; Plane, J. M. C. Absorption cross sections and kinetics of formation of AlO at 298 K. *Chem. Phys. Lett.* **2017**, *675*, 56−62.

(23) Gaydon, A. G. Green and Orange Band Spectra of CaOH, CaOD and Calcium Oxide. *Proc. R. Soc. London, Ser. A* **1955**, *231* (1187), 437−445.

(24) Kramida, A.; Ralchenko, Y.; Reader, J.; Team, N. A. *NIST Atomic Spectra Database, Version 5.3*; National Institute of Standards and Technology (NIST): Gaithersburg, MD, 2015; https://www.nist.gov/pml/atomic-spectra-database.

(25) Stewart, J. T.; Sullivan, M. N.; Heaven, M. C. Near UV bands of jet-cooled CaO. *J. Mol. Spectrosc.* **2016**, *322*, 18−21.

(26) Pereira, R.; Levy, D. H. Observation and spectroscopy of high-lying states of the CaOH radical: Evidence for a bent, covalent state. *J. Chem. Phys.* **1996**, *105* (22), 9733−9739.

(27) Western, C. M. *PGOPHER, Version 9.1*; University of Bristol Research Data Repository: Bristol, U.K., 2016; DOI: 10.5523/bris.1nz94wvrfzzdo1d67et0t4v4nc.

(28) Dick, M. J.; Sheridan, P. M.; Wang, J. G.; Yu, S.; Bernath, P. F. Optical−optical double resonance spectroscopy of the transition of CaOH. *J. Mol. Spectrosc.* **2006**, *240* (2), 238−243.

(29) Coxon, J. A.; Li, M.; Presunka, P. I. Laser fluorescence excitation spectroscopy of CaOH and CaOD: The $A^2\Pi-X^2\Sigma^+$ (100)−(000) band system and the (100)−(020) Fermi resonance. *J. Mol. Spectrosc.* **1991**, *150* (1), 33−45.

(30) Cox, J. D.; Wagman, D. D.; Medvedev, V. A. *CODATA Key Values for Thermodynamics*; Hemisphere Publishing Corporation: New York, 1989.

(31) Yurchenko, S. N.; Blissett, A.; Asari, U.; Vasilios, M.; Hill, C.; Tennyson, J. ExoMol molecular line lists—XIII. The spectrum of CaO. *Mon. Not. R. Astron. Soc.* **2016**, *456* (4), 4524−4532.

(32) Husain, D.; Roberts, G. Energy pooling from Ca[4s4p(^{3}P)] and Ca[4s3d($^1D_2$)] studied by time-resolved atomic emission following

DOI: 10.1021/acsearthspacechem.7b00072
ACS Earth Space Chem. 2017, 1, 431−441

pulsed dye-laser excitation. *J. Chem. Soc., Faraday Trans. 2* **1986**, *82* (11), 1921−1933.
(33) Diffenderfer, R. N.; Dagdigian, P. J.; Yarkony, D. R. Spin-forbidden radiative transitions in atomic calcium. *J. Phys. B: At. Mol. Phys.* **1981**, *14* (1), 21.
(34) Irvin, J. A.; Dagdigian, P. J. Chemiluminescence from the Ca(4s3d ^{1}D) + O_2 reaction: Absolute cross sections, photon yield, and CaO dissociation energy. *J. Chem. Phys.* **1980**, *73* (1), 176−182.
(35) Irvin, J. A.; Dagdigian, P. J. A study of the reactions Ca(^{1}S,^{3}P$_0$, and ^{1}D)+N_2O under single-collision conditions and at higher pressures: Chemiluminescence cross sections, photon yields, and collisional energy transfer in CaO* by N_2O. *J. Chem. Phys.* **1981**, *74* (11), 6178−6187.
(36) Glowacki, D. R.; Liang, C.-H.; Morley, C.; Pilling, M. J.; Robertson, S. H. MESMER: An Open-Source Master Equation Solver for Multi-Energy Well Reactions. *J. Phys. Chem. A* **2012**, *116* (38), 9545−9560.
(37) Robertson, S. H.; Glowacki, D. R.; Liang, C.-H.; Morley, C.; Shannon, R.; Blitz, M.; Pilling, M. J. *MESMER (Master Equation Solver for Multi-Energy Well Reactions)*; http://sourceforge.net/projects/mesmer.
(38) Frisch, M. J.; Trucks, G. W.; Schlegel, H. B.; Scuseria, G. E.; Robb, M. A.; Cheeseman, J. R.; Scalmani, G.; Barone, V.; Mennucci, B.; Petersson, G. A.; Nakatsuji, H.; Caricato, M.; Li, X.; Hratchian, H. P.; Izmaylov, A. F.; Bloino, J.; Zheng, G.; Sonnenberg, J. L.; Hada, M.; Ehara, M.; Toyota, K.; Fukuda, R.; Hasegawa, J.; Ishida, M.; Nakajima, T.; Honda, Y.; Kitao, O.; Nakai, H.; Vreven, T.; Montgomery, J. A., Jr.; Peralta, J. E.; Ogliaro, F.; Bearpark, M. J.; Heyd, J.; Brothers, E. N.; Kudin, K. N.; Staroverov, V. N.; Kobayashi, R.; Normand, J.; Raghavachari, K.; Rendell, A. P.; Burant, J. C.; Iyengar, S. S.; Tomasi, J.; Cossi, M.; Rega, N.; Millam, N. J.; Klene, M.; Knox, J. E.; Cross, J. B.; Bakken, V.; Adamo, C.; Jaramillo, J.; Gomperts, R.; Stratmann, R. E.; Yazyev, O.; Austin, A. J.; Cammi, R.; Pomelli, C.; Ochterski, J. W.; Martin, R. L.; Morokuma, K.; Zakrzewski, V. G.; Voth, G. A.; Salvador, P.; Dannenberg, J. J.; Dapprich, S.; Daniels, A. D.; Farkas, Ö.; Foresman, J. B.; Ortiz, J. V.; Cioslowski, J.; Fox, D. J. *Gaussian 09*; Gaussian, Inc.: Wallingford, CT, 2009.
(39) Troe, J. Predictive possibilities of unimolecular rate theory. *J. Phys. Chem.* **1979**, *83* (1), 114−126.
(40) Burkholder, J. B.; Sander, S. P.; Abbatt, J.; Barker, J. R.; Huie, R. E.; Kolb, C. E.; Kurylo, M. J.; Orkin, V. L.; Wilmouth, D. M.; Wine, P. H. *Chemical Kinetics and Photochemical Data for Use in Atmospheric Studies*; Jet Propulsion Laboratory, California Institute of Technology: Pasadena, CA, 2015; Evaluation 18, JPL Publication 15-10, http://jpldataeval.jpl.nasa.gov.
(41) Troe, J.; Ushakov, V. G. Representation of "Broad" Falloff Curves for Dissociation and Recombination Reactions. *Z. Phys. Chem.* **2014**, *228* (1), 1.

DOI: 10.1021/acsearthspacechem.7b00072
ACS Earth Space Chem. 2017, 1, 431−441